

“Hare and Hounds” Tests of Helioseismic Holography

A.C. Birch · K.V. Parchevsky · D.C. Braun ·
A.G. Kosovichev

Received: 11 November 2010 / Accepted: 15 May 2011 / Published online: 21 July 2011
© Springer Science+Business Media B.V. 2011

Abstract We use the output of numerical wave-propagation simulations as synthetic data for “hare and hounds” tests of helioseismic holography. In the simple non-magnetic models examined here, we show that when the inversion method includes a consistent treatment of the filtering applied during the data analysis the inversions for the subsurface sound speed are qualitatively correct.

Keywords Sun: helioseismology · Sun: interior · Sun: oscillations

1. Introduction

Local helioseismology is a set of tools for studying the three-dimensional structure of the solar interior (for recent reviews see Gizon and Birch, 2005; Gizon, Birch, and Spruit, 2010; Kosovichev, 2011). Sunspots are one of the most important targets for local helioseismology; there have been many estimates of the wave speed underneath sunspots and active regions (*e.g.*, Fan, Braun, and Chou, 1995; Kosovichev, 1996; Kosovichev, Duvall, and Scherrer, 2000; Jensen *et al.*, 2001; Zhao and Kosovichev, 2003; Basu, Antia, and Bogart, 2004; Crouch *et al.*, 2005; Couvidat, Birch, and Kosovichev, 2006; Kosovichev and Duvall, 2006; Bogart *et al.*, 2008; Kosovichev, 2009; Gizon *et al.*, 2009; Moradi *et al.*, 2010; Kosovichev, 2011; Cameron *et al.*, 2011). In many (although not all) of these studies, sound speed is used a proxy for all effects that cause changes in wave speed; *e.g.* changes in temperature and/or magnetic fields.

As a small step toward understanding the ability of local helioseismology to accurately infer local changes in the sound speed, we show here simple “hare and hounds” tests – that is, the analysis of artificial data without foreknowledge of the model used to create the

A.C. Birch (✉) · D.C. Braun
CoRA Division, NWRA, 3800 Mitchell Lane, Boulder, CO 80301, USA
e-mail: aaronb@cora.nwra.com

K.V. Parchevsky · A.G. Kosovichev
HEPL, Stanford University, Stanford, CA 94305, USA

data – of helioseismic holography (Lindsey and Braun, 2000). In particular, we use synthetic data from a numerical wave-propagation simulation to show, in a few simple example non-magnetic problems, that helioseismic holography can be used to infer local subsurface changes in sound speed. We shall show that inversions can be carried out from travel-time shifts measured using phase-speed filters or ridge filters. These simple tests show that it is possible to produce forward models that account for the details of the filtering used in the course of measuring travel-time shifts. Similar testing using the same simulation data has been done for the time–distance helioseismology technique by Zhao, Parchevsky, and Kosovichev (2011).

Here we will consider two types of sound-speed models, both motivated by inferences of wave-speed variations associated with sunspots: two-layer models (*e.g.* Kosovichev, Duvall, and Scherrer, 2000) in which there is a near-surface reduction in wave speed overlying a layer of increased sound speed, and one-layer models (*e.g.*, Fan, Braun, and Chou, 1995) which consist of a near-surface enhancement of the sound speed. Tests with these sound-speed models serve two purposes:

- i*) These models resemble the wave-speed structures inferred for some sunspots and thus provide tests of the ability of inversions to retrieve the relevant spatial scales.
- ii*) In addition, these tests provide a baseline against which future inversions (*e.g.* with models including magnetic fields) may be compared.

In Section 2 we describe the synthetic data used in this article. In Section 3 we describe the methods for measuring travel-time shifts and show travel-time maps for the synthetic data. The sensitivity (kernel) functions for the inversion are described in Section 4, and the inversion methods and results are given in Section 5. We conclude with a discussion of the implications of the results shown here (Section 6).

2. Synthetic Data

Simulations of wave propagation are an important tool for testing methods of local helioseismology. These simulations provide wave fields that are consistent with known models for conditions (*i.e.* models for the sound speed, density, pressure, *etc.*) in the solar interior. Local helioseismology can be applied to these synthetic wavefields and the results compared with the known physical conditions in the interior of the model.

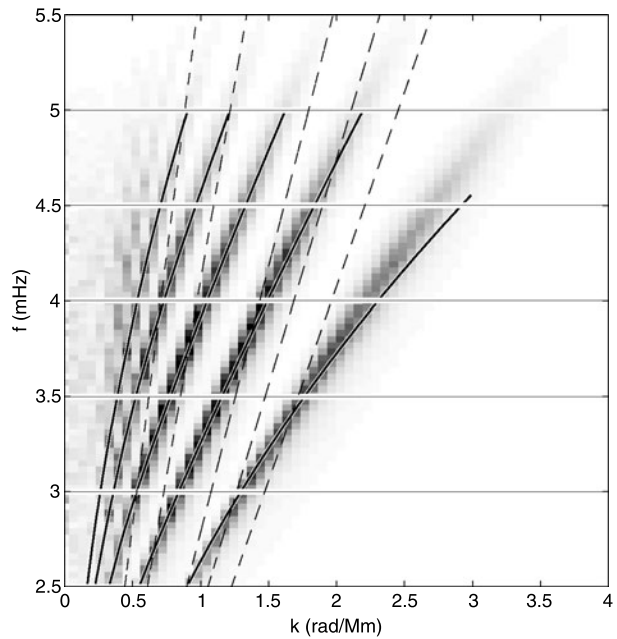
We use the linear wave-propagation code of Parchevsky, Zhao, and Kosovichev (2008) to generate artificial data. The simulation computes the propagation of small-amplitude waves through a specified model for the solar interior. The model consists of a background component that is intended to model the quiet Sun together with a local perturbation to the sound speed at constant pressure and density. In the examples shown here, the form of the sound-speed perturbation is chosen to be

$$\delta c^2/c_0^2 = f(z) \exp(-r^2/R^2), \quad (1)$$

where r is horizontal distance from the center of the simulation domain, $R = 20$ Mm is the horizontal length scale of the perturbation, z is height above the photosphere, $c_0(z)$ is the unperturbed (“quiet-Sun”) sound speed, and $\delta c^2(r, z)$ is the perturbation to the square of the sound speed. Here we show results for two different choices of $f(z)$.

- i*) For the first case, the “two-layer” model, the function $f(z)$ is chosen to resemble the change in the sound speed inferred from time–distance helioseismology of sunspots (*e.g.*, Kosovichev, Duvall, and Scherrer, 2000) and is shown in Figure 9.

Figure 1 Power spectrum of the vertical velocity at 300 km above the photosphere from the simulation with the two-layer sound-speed perturbation. The resonant frequencies of Model S are shown as black lines. There is qualitative agreement with the Model S resonant frequencies; although there is some disagreement for the f -mode ridge at frequencies above about 4 mHz. Here, we do not use the f mode and thus we do not expect this deviation from Model S to be important in the current work. The dashed lines show the central phase speeds of the phase-speed filters TD1 through TD5.



- ii) For the second case, the “one-layer” model, we choose $f(z) = \exp[-(z/D)^2]$ with $D = 1$ Mm (see, *e.g.*, Fan, Braun, and Chou, 1995).

The simulations are driven by a stochastic forcing function as discussed by Parchevsky and Kosovichev (2009). We take the vertical velocity at a height of 300 km above the photosphere from the simulation as synthetic data.

Figure 1 shows the power spectrum of the synthetic data for the two-layer model. Throughout most of the k - ω diagram, the resonance frequencies in the simulation show general agreement with those of Model S (Christensen-Dalsgaard *et al.*, 1996). There is some disagreement in the position of the f -mode ridge at frequencies above about 4 mHz. This disagreement may be caused by the interaction of the f mode with the top of the simulation domain. The f mode is not used in the current study, and thus we do not expect this deviation to substantially affect the work carried out here.

3. Travel-Time Measurements

Filtering in k - ω space has been applied in many time–distance measurements (*e.g.*, Duvall *et al.*, 1997; Kosovichev, Duvall, and Scherrer, 2000; Zhao, Kosovichev, and Duvall, 2001; Couvidat, Birch, and Kosovichev, 2006; Jackiewicz, Gizon, and Birch, 2008; Gizon *et al.*, 2009; Zhao, Kosovichev, and Sekii, 2010, among a great many others) and also in measurements made with helioseismic holography (*e.g.*, Braun and Birch, 2006, 2008; Birch *et al.*, 2009). Some of the motivations for this filtering are to permit measurements at very short distances (*e.g.*, Duvall *et al.*, 1997), improve signal-to-noise ratios (*e.g.*, Couvidat and Birch, 2006), and/or to isolate particular wave modes (*e.g.*, Braun and Birch, 2006). In this section we show the results of measurements using both phase-speed filters and ridge filters; this will allow comparison of inversion results for these two classes of filters.

We use the following general data-analysis procedure: apply the ridge or phase-speed filter to the synthetic wavefield (Section 3.1), measure the local control correlations using the Green's functions described by Lindsey and Braun (2000) (Section 3.2), apply frequency filters to the resulting local control correlations (Section 3.3), and then measure travel-time shifts from the filtered local control correlations (Section 3.4). The end result of the procedure is a set of travel-time maps, one for each phase or ridge filter combined with a frequency band-pass filter.

3.1. Ridge and Phase-Speed Filters

We use the ridge filters described by Braun and Birch (2008). These filters isolate waves of a particular radial order n ; here we look at the cases of $n = 1, 2, 3, 4$. Notice that we are not using the f mode in the current study. For the phase-speed filters we use filters TD1 (central phase speed of 12.8 km s^{-1}) through TD5 (central phase speed of 35.5 km s^{-1}) from Couvidat, Birch, and Kosovichev (2006). For each filter, there is a corresponding pupil function that is employed in the data analysis (for descriptions of the pupil functions see Couvidat, Birch, and Kosovichev, 2006).

3.2. Local Control Correlations

The definition of the local control correlation, the holography Green's functions, and holography pupils (which depend on the filters) are described in detail by Braun and Birch (2008). The local control correlation is analogous to the center–annulus cross-covariance employed in time–distance helioseismology (for a review see Gizon and Birch, 2005).

3.3. Frequency Filtering

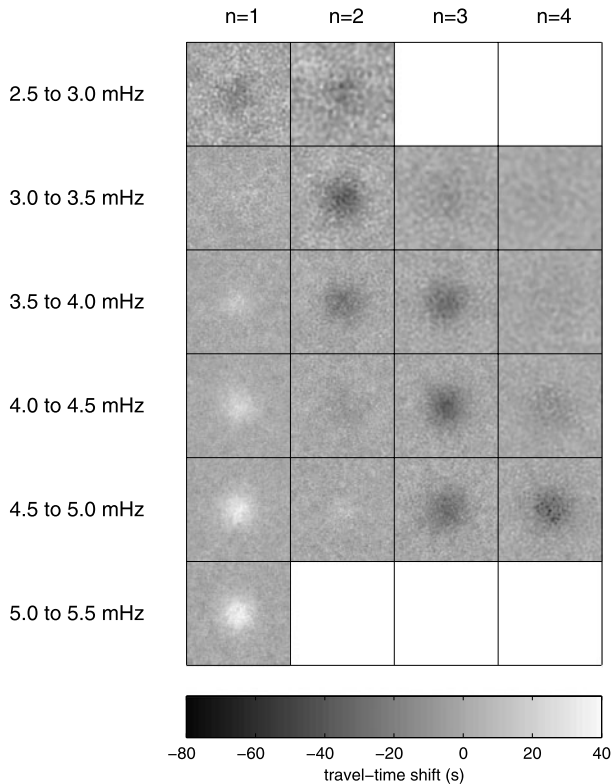
Braun and Birch (2006) showed that travel-time shifts measured in sunspots are strongly dependent on the temporal frequencies that are used in the measurements. In addition, in general, waves with different frequencies have different sensitivities to local changes in sound speed (see Section 4). For both of these reasons, we apply filters to isolate small ranges in frequency. We chose to use band-pass filters centered at 2.75, 3.25, 3.75, 4.25, and 4.75 mHz with widths all equal to 0.5 mHz. This array of filters was selected to give an, apparently reasonable, balance between signal-to-noise ratio and resolution in the frequency domain.

3.4. Definition of Travel-Time Shifts

In general, there are many methods for measuring travel-time shifts from local control correlations (or time–distance covariances): Gaussian-wavelet fitting (Duvall *et al.*, 1997), one-parameter fitting (Gizon and Birch, 2002), linearization of the one-parameter fitting method (Gizon and Birch, 2004), and the phase method (Lindsey and Braun, 2000). A review of the first three of these methods is given by Couvidat *et al.* (2010).

In all cases, we measure the travel-time shifts relative to the spatial average of the local control correlation over the region further than 36 Mm from the center of the spatial domain, (*i.e.* in the region in which the sound-speed perturbation is essentially zero, see Figures 2 and 4). For the simulations discussed here, the one-parameter and Gaussian-wavelet methods give results that agree to within a few percent. The phase method gives results that typically agree with the other two methods within about 10%. The sensitivity functions (Section 4

Figure 2 Travel-time shifts measured using ridge filters in combination with frequency band-pass filters for the two-layer model. The maps are arranged with the radial order of the ridge filters increasing from left to right from $n = 1$ to $n = 4$. The central frequency of the band-pass filters increases from 2.75 mHz in the top row to 5.25 mHz in the bottom row. Notice that the travel-time shifts are not a simple function of either the radial order or the central frequency. For example, for the $n = 1$ case, the travel-time shifts are negative at low frequency and positive at high frequency. This trend is seen in the $n = 2$ case as well. For $n = 3$ and $n = 4$ the travel-time shifts are mostly negative. In some cases, (e.g. $n = 3$, $f = 2.5 - 3.0$ mHz) the maps are dominated by noise and not shown. Each map covers an area of $96 \times 96 \text{ Mm}^2$.



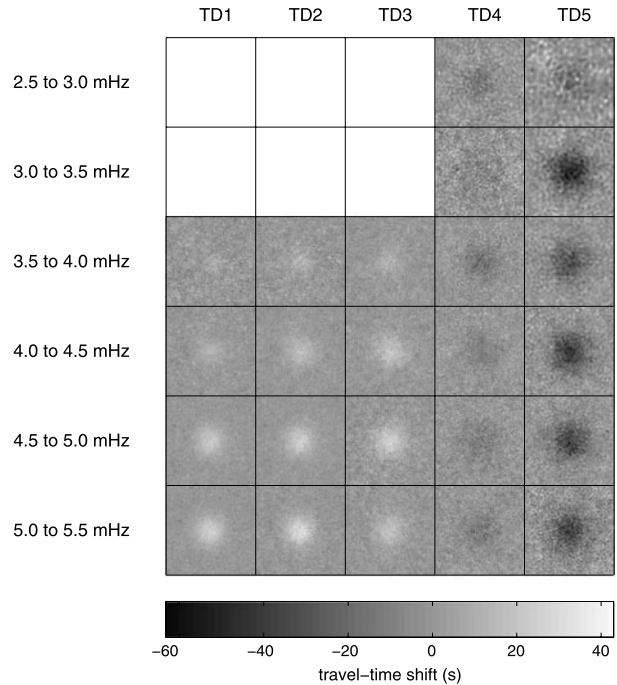
and Appendix) are derived under the assumption that travel-time shifts are measured using the phase method, and for the remainder of the article we employ this method. Notice that in the case of MDI measurements of sunspots, the situation is more complicated and different methods of measuring travel-time shifts can yield significantly different results (e.g., Couvidat *et al.*, 2010).

3.5. Travel-Time Maps

Figure 2 shows maps of travel-time shifts measured using ridge filters together with frequency band-pass filters. We find that the travel-time shifts depend on both the radial order and the central frequency of the band-pass filter. For example, for the case $n = 1$, we see negative travel-time shifts, (*i.e.* the waves are moving more quickly than in the reference) at low frequency and positive travel-time shifts at high frequency. This pattern is repeated in the $n = 2$ case, although the transition from negative to positive travel-time shifts happens at a different frequency. This behavior is a consequence of the frequency dependence of the mode structure and will be discussed in Section 5.

Figure 3 shows maps of travel-time shifts for the case of phase-speed filters combined with band-pass frequency filters. The pattern here is more obvious than in the case of the ridge-filtered measurements (Figure 2). We see that at low phase speeds (TD1, TD2, and TD3) the travel-time shifts are positive for all frequencies. At the higher phase speeds (TD4 and TD5) the travel-time shifts are negative. This general pattern is what would be expected for the two-layer structure of the sound-speed perturbation.

Figure 3 Travel-time shifts measured using phase-speed filters in combination with frequency band-pass filters for the two-layer model. The maps are arranged with the central phase speed of the filter increasing from 12.8 km s^{-1} (TD1) in the left-most column to 35.5 km s^{-1} (TD5) in the right-most column. As in Figure 2, the central frequency of the band-pass filter increases from 2.75 mHz in the top row to 5.25 mHz in the bottom row. For filters TD1, TD2, and TD3 the travel-time shifts are largely positive, while for TD4 and TD5 they are mostly negative. Each map covers an area of $96 \times 96 \text{ Mm}^2$.



Figures 4 and 5 show measurements from the one-layer model. For the case of ridge filters (Figure 4) the travel-time shifts caused by the increased sound speed are mostly negative and increase in magnitude with increasing frequency. The maps at lower frequency and for $n = 2$ and $n = 3$ are dominated by noise. The situation is similar for the case of phase-speed filters (Figure 5). In particular, even at the lowest phase speeds we see negative travel-time shifts. This is qualitatively different than was seen by Birch *et al.* (2009) (which was based on different synthetic data). Birch *et al.* (2009) showed that travel-time shifts measured using phase-speed filters at low phase speeds are sensitive to the detailed shape of the power spectrum (in particular the power in between the p_1 and f ridges).

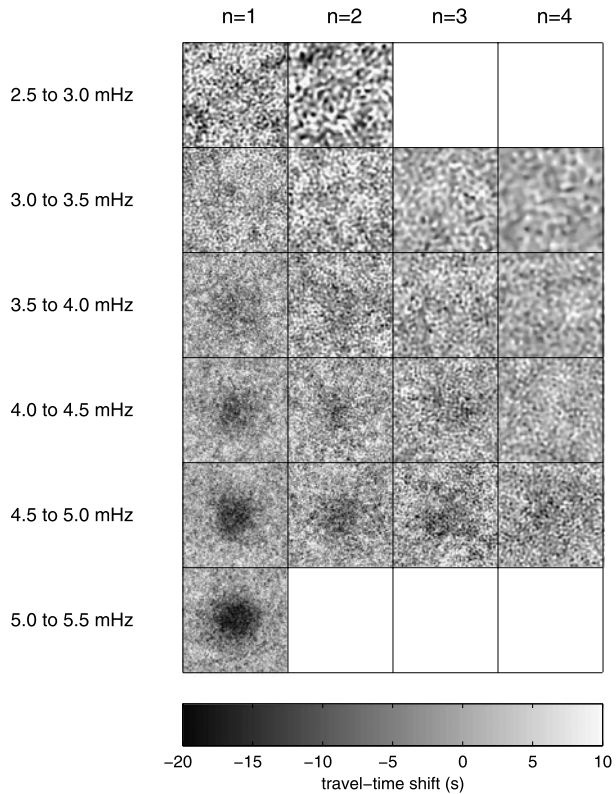
4. Sensitivity Functions

In the Appendix, we generalize the Born-approximation calculations of Birch, Kosovichev, and Duvall (2004) to compute the linear sensitivity of travel-time shifts measured from local control correlations to weak local changes in the sound speed. The result of this calculation is a set of sensitivity functions (kernels) that satisfy

$$\delta\tau(\mathbf{r}) = \iiint K(\mathbf{r}' - \mathbf{r}, z) \delta c^2(\mathbf{r}', z) / c_0^2(z) d\mathbf{r}' dz, \quad (2)$$

where \mathbf{r} and \mathbf{r}' are horizontal positions, $\delta\tau$ is a map of travel-time shifts for a particular choice of filters, z is height (with the photosphere located at $z = 0$), $c_0(z)$ is the sound speed in the reference model (Model S: Christensen-Dalsgaard *et al.*, 1996), and δc^2 is the perturbation to the square of the sound speed. For each combination of filters (*e.g.* combination of ridge and band-pass frequency filters) there is a different kernel function $[K]$.

Figure 4 Travel-time shifts measured using ridge filters in combination with frequency band-pass filters for the one-layer model. The maps are arranged with the radial order of the ridge filters increasing to the right from $n = 1$ to $n = 4$. The central frequency of the band-pass filters increases from 2.75 mHz in the top row to 5.25 mHz in the bottom row. Each map covers an area of $96 \times 96 \text{ Mm}^2$.



In the rest of this article, we discretize the perturbation to the square of the sound speed as

$$\delta c^2(\mathbf{r}, z)/c_0^2(z) = \sum_{\mathbf{k}, i} m_i(\mathbf{k})\phi_i(z)e^{i\mathbf{k}\cdot\mathbf{r}} \tag{3}$$

where the $\phi_i(z)$ are basis functions that have a value of one when $z_k \leq z < z_{k+1}$ and zero otherwise. The grid $\{z_k\}$ consists of 35 points that are uniformly spaced in acoustic depth and cover the range from -9.7 Mm to 0.5 Mm . We will see in the inversion results shown later that the discretization in depth is not causing significant loss of information. The \mathbf{k} are horizontal wave vectors, and the sum over \mathbf{k} is proportional to the inverse Fourier transform in the horizontal directions (here we employ the Fourier convention of Gizon and Birch, 2004). We will use the symbol h_k to denote the grid spacing in k -space; here $h_k = 0.0654 \text{ rad Mm}^{-1}$.

Figure 6 shows one example of a function K for the case of the $n = 3$ ridge filter together with a band-pass frequency filter centered at 4.25 mHz with a width of 0.5 mHz. The sensitivity is strongly localized near the focus point, with a full-width at half maximum that is about 2.5 Mm, which is slightly less than half of the dominant wavelength (about 7 Mm). For horizontally uniform changes in sound speed, the depth dependence of the sensitivity is approximately proportional to $\rho_0(z)\|\nabla \cdot \xi_n(k; z)\|^2$, where ρ_0 is the quiet-Sun density and $\xi_n(k; z)$ is the displacement eigenfunction for the mode with radial order n and horizontal wavenumber k , as would be expected from global-mode theory (e.g. Gough and Thompson, 1991).

Figure 5 Travel-time shifts measured using phase-speed filters in combination with frequency band-pass filters for the one-layer model. The maps are arranged with the central phase speed of the filter increasing from 12.8 km s^{-1} in the left-most column to 35.5 km s^{-1} in the right-most column. Each map covers an area of $96 \times 96 \text{ Mm}^2$.

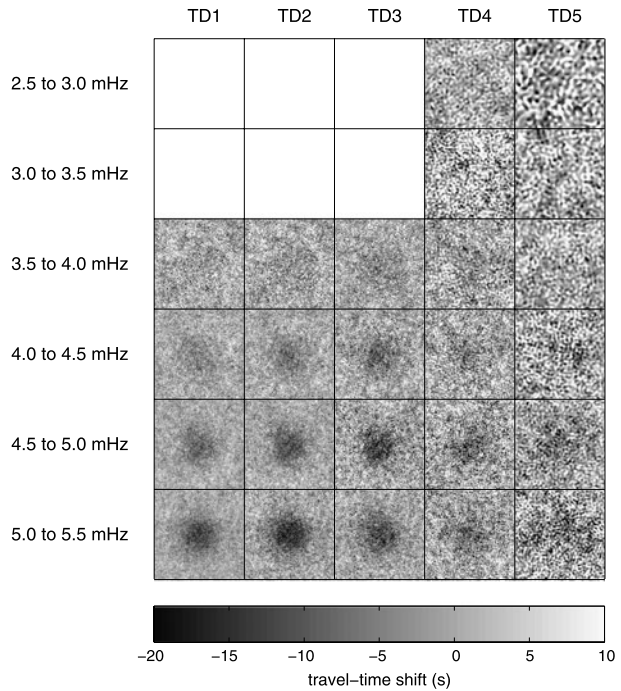


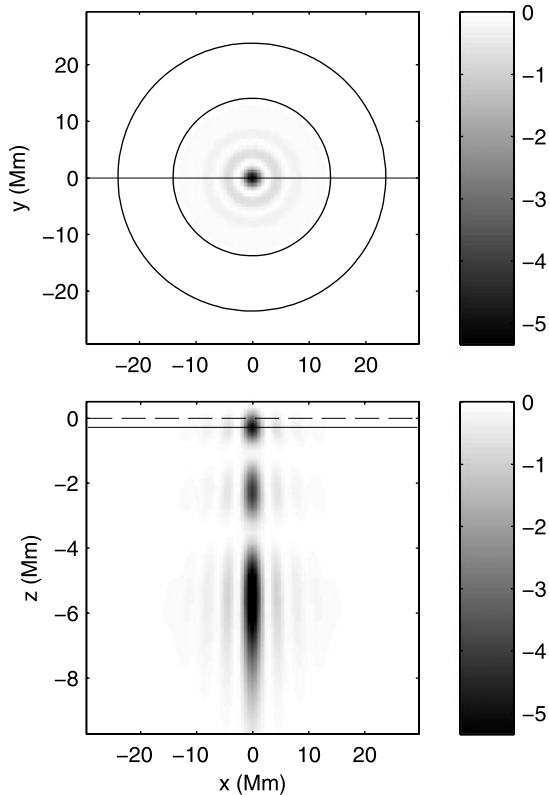
Figure 7 shows the horizontal integrals (*i.e.* sensitivity functions for the case when δc^2 is a function of z alone) for all of the ridge-filtered measurements shown in Figures 2 and 4. The depth structure of the kernels is what would be expected from normal-mode theory. At fixed radial order, the sensitivity functions are shallower at high frequency than at low frequency. This is because the lower turning point moves upwards with increasing frequency at fixed radial order. In all cases, there is very little sensitivity to changes in sound speed above the photosphere. The eigenfunction calculation that is the basis of the computation of sensitivity functions (Birch, Kosovichev, and Duvall, 2004) employs an upper boundary condition of zero Lagrangian pressure perturbation. This boundary condition is very likely inaccurate at frequencies near the acoustic cutoff frequency (roughly 5.5 mHz). In Section 5 we will discuss some possible consequences of this approximation.

Figure 8 is the same as Figure 7 except that it shows the horizontal integrals of the kernels for the phase-speed filtered measurements. The TD1 and TD2 filters are dominated by the p_1 mode. The TD3 filter is also mostly sensitive to the $n = 1$ mode, except for the frequency range 5–5.5 mHz, where the $n = 2$ mode contributes as well. For the TD4 and TD5 cases, the situation is more complicated, with different radial orders appearing in those filters at different frequencies.

5. Inversion Results

The inversions we have carried out are standard MCD inversions (Jacobsen *et al.*, 1999) with a 1D RLS depth inversion at each horizontal wavevector. Each 1D RLS inversion is regularized by the depth integral of the square of the solution m . The regularization parameter $[\lambda]$ is a function of the horizontal wavenumber and is given by $\lambda^2 = \lambda_1^2 + k^2 \lambda_2^2$ (Couvidat

Figure 6 Example kernel for the ridge filter with $n = 3$ and the frequency range of 4 to 4.5 mHz. The top panel shows a slice at about 200 km below the photosphere. The two black circles show the inner and outer radii of the pupil used in the travel-time measurement. The bottom panel shows a vertical slice through the kernel at $y = 0$. The horizontal dashed line shows the height of the photosphere and the horizontal solid line shows the height at which the slice in the top panel is taken. The gray scale shows the value of the kernel in units of seconds (after discretization into cells in three dimensions; see the Appendix). The depth dependence of the kernel is roughly $\rho_0 \|\nabla \cdot \xi\|^2$ where ξ is the displacement eigenfunction of the $n = 3$ mode at the mean frequency of the power after the band-pass frequency filter has been applied.



et al., 2005). Also following Couvidat *et al.* (2005), the inversion accounts for the full error-covariance matrix, and this covariance is estimated using the method of Gizon and Birch (2004). The error estimates for the inversion results are computed by the formal propagation of errors.

Figure 9 shows vertical slices through four example inversions with different regularization parameters. We see that the inversion results depend on the choice of regularization. For small λ_1 and λ_2 , the solutions are oscillatory in depth as well as in the horizontal directions. It is possible to choose the regularization parameters to obtain inversion results that are smooth in both z and the horizontal directions, or smooth in only the horizontal or vertical directions.

Figure 10 shows a comparison of an example inversion carried out using ridge filters and $(\lambda_1, h_k \lambda_2) = (0.2, 0.2) \text{ Mm}^{-1/2}$ with the known model for the perturbation to the sound speed. In this case, the inversion has retrieved the basic structure of the true model. The lower-left panel of Figure 10 shows, however, that the inversion has missed several features of the true model. In particular, the inversion does not do well near the surface [$z = 0$] and at depths greater than 5 Mm. This is because the kernels are small in these regions. It may be that the zero Lagrangian pressure-perturbation boundary condition employed as part of the kernel calculation results in kernels that are too small in the near-surface layers. To test if errors in the kernels at high frequencies cause systematic errors, we repeated the inversion shown here although with the measurements at frequencies above 4.5 mHz removed. The results did not change substantially. The source of the large bias in the inversion at -2 Mm is not clear. The lower-right panel of Figure 10 shows the comparison of some measured travel-

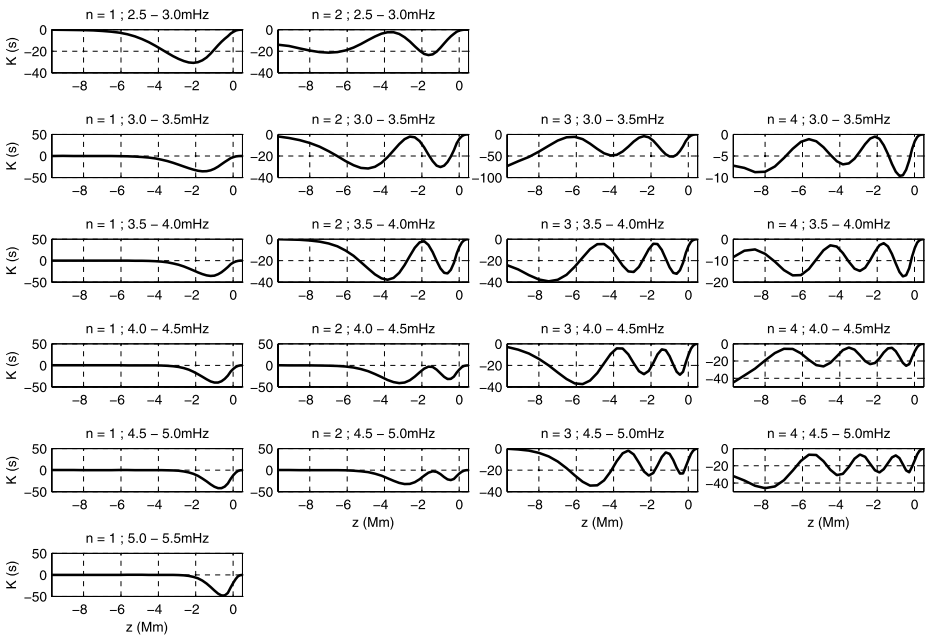


Figure 7 Horizontal integrals of Born-approximation travel-time kernels for measurements made using ridge filters and frequency filters. The kernels reflect the depth dependence of the mode eigenfunctions that contribute to each measurement. At fixed radial order, the kernels extend to larger depths for lower frequencies; this is expected as the lower turning-point depth increases with decreasing frequency at fixed radial order.

time shifts and the corresponding predictions of the inversion, (*i.e.* the travel-time shifts that would be expected given the model m). We see that the inversion is largely reproducing the measurements, although because of the regularization the model travel-time shifts are of somewhat smaller amplitude.

Figure 11 shows an example inversion result for the two-layer model and the case of the phase-speed filters. The situation is very similar to that seen in Figure 10. Again the inversion does not do well near the surface and at depths below about 5 Mm. However, as with the case of the ridge filters, the basic structure of the inversion result is roughly consistent with the true model. Also, as with the case of the ridge filters, the inversion produces travel-time shifts that are roughly consistent with the input travel-time shifts.

Figure 12 shows a few example averaging kernels for the inversion shown in Figure 11. The averaging kernels show that the horizontal resolution decreases as the depth increases. The averaging kernels show near-surface sidelobes. These sidelobes could perhaps be reduced by using an OLA inversion (*e.g.*, Jackiewicz, Gizon, and Birch, 2008, in the context of time–distance helioseismology) in place of the RLS inversion employed here.

Figure 13 shows an example inversion for the case of the one-layer model and the ridge filters. The inversion has recovered the correct basic structure. The amplitude of the solution is too small, this is a result of the choice of regularization parameters. As expected, the travel-time shifts predicted from the inversion result (lower-right panel of Figure 13) are somewhat smaller in amplitude than the measured travel-time shifts. Again, this is due to the regularization. For other choices of the regularization parameters, it is possible to obtain solutions that are larger in amplitude at the cost of noise in the inversion result.

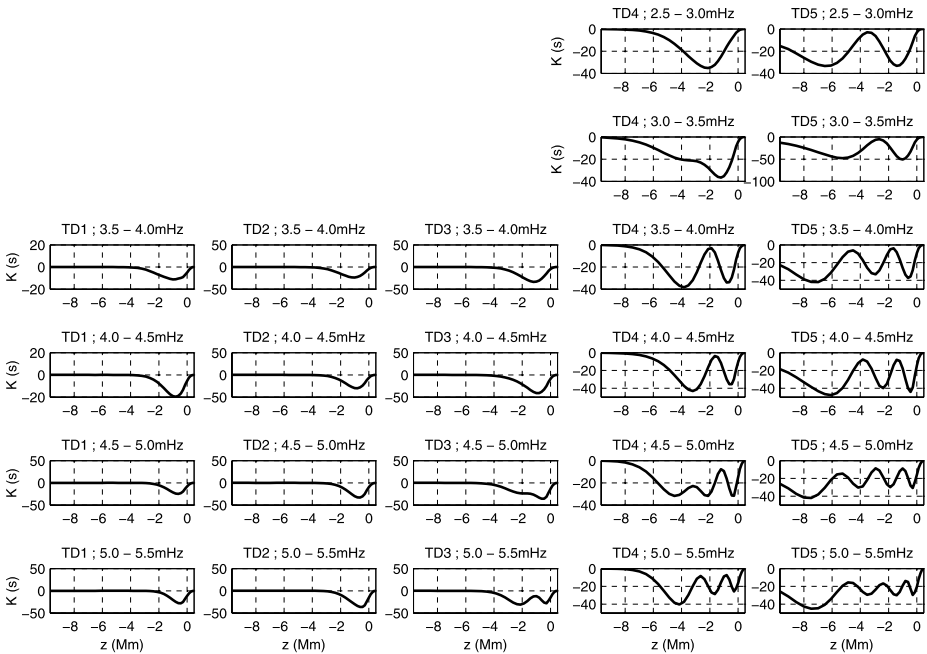


Figure 8 Horizontal integrals of Born-approximation travel-time kernels for the measurements made using phase-speed filters and frequency filters. Notice that the kernels reflect the depth dependence of the mode eigenfunctions that contribute to each measurement. For example, the filters TD1 and TD2 are dominated by the $n = 1$ mode, while the TD3 filters selects the $n = 1$ mode at low frequencies and the $n = 2$ mode at high frequency.

Figure 14 shows an example inversion for the case of the one-layer model and the phase-speed filters. This situation is very similar to the case of the ridge filters: the solution has the correct basic shape but the amplitude is somewhat too small. This is the price of regularization using the amplitude of the solution.

6. Discussion

We used the results of two numerical wave-propagation simulations as synthetic data for testing sound-speed inversions of travel-time shifts measured using helioseismic holography. In all cases, the inversions were carried out using sound-speed kernels computed in the Born approximation. In all of the examples shown here, the inversions are able to recover the qualitative structure of the known perturbations to the background solar model. There were no major qualitative differences in the inversions carried out using the ridge filters and phase-speed filters.

The two-layer model shown here produces travel-time maps that are in many ways similar to the results of measurements of sunspots made using helioseismic holography. They are, however, not identical. For example, p_1 -ridge-filtered measurements of sunspots typically produce negative travel-time shifts (e.g. Figure 8 of Braun and Birch (2008) and Figure 7 of Gizon *et al.* (2009)) rather than the positive travel-time shifts seen here. In addition, in sunspots there is typically a change of sign between the phase-speed filtered holography measurements (at the lowest phase speeds) made at low frequency and those at high

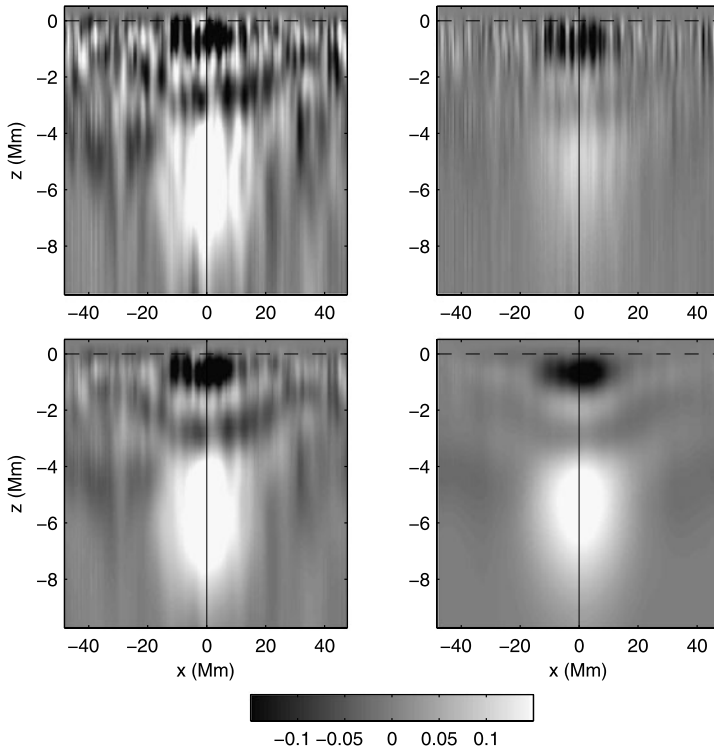


Figure 9 Example inversion results for the travel-time shifts measured using ridge filters for the two-layer model shown in Figure 2 and the kernels shown in Figure 7. The gray scale shows $\delta c^2/c^2$. The regularization parameters for the top-left panel are $(\lambda_1, \lambda_2 h_k) = (0.2, 0.02) \text{ Mm}^{-1/2}$, top-right $(1.0, 0.02) \text{ Mm}^{-1/2}$, bottom-left $(0.2, 0.05) \text{ Mm}^{-1/2}$, and bottom-right $(0.2, 0.2) \text{ Mm}^{-1/2}$.

frequency (*e.g.*, Braun and Birch, 2006, 2008; Gizon *et al.*, 2009); this was seen using time–distance analysis as well by Couvidat and Rajaguru (2007). It will be important to develop model sunspots that can reproduce these observations.

The inversions are not able to recover the true sound-speed structure near and above the photosphere as the travel-time measurements have very little sensitivity in this region; this may be in part due to the unrealistic upper boundary condition (zero Lagrangian pressure perturbation at about 500 km above the photosphere) at high frequency employed as part of the calculation of the sensitivity functions. In addition, the inversion severely underestimates the amplitude of the sound-speed perturbations at depths below about five Mm in the case of the two layer model. This is due in part to the choice of regularization method.

The generalization of the simple tests shown here to magnetic sunspot models is important. Here, we have only shown a self-consistent formalism for inversions for helioseismic-holography measurements of local variations in the sound speed. The extent to which this formalism can be applied to the case of sunspot seismology is currently being studied.

Acknowledgements The work of ACB and DCB was supported by NASA contracts NNH09CE41C and NNH09CF68C. KP and AGK acknowledge support from NASA grants NNX07AP61 and NAS5-02139. We thank A. Crouch for calculations using translation-invariant models that helped verify the inversion method.

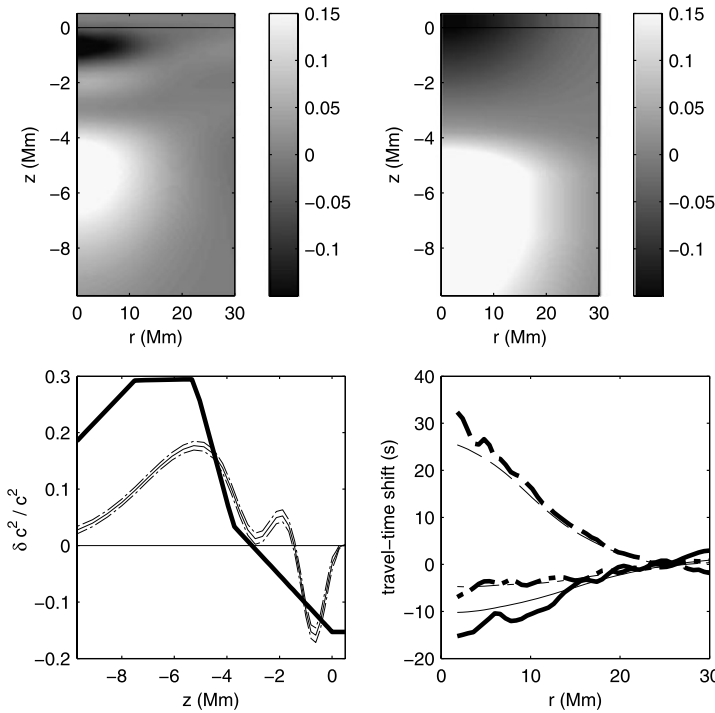


Figure 10 Comparison of an inversion solution with the true two-layer model for the case of the ridge-filtered measurements and $(\lambda_1, h_k \lambda_2) = (0.2, 0.2) \text{ Mm}^{-1/2}$. The top-left panel shows the azimuthal average of the inversion result. The top-right panel shows the true model. The bottom-left panel shows the inferred model (light line with error estimates) and true model (heavy line) at the center of the “spot” region. The bottom-right panel shows the azimuthal averages of the travel-time maps (heavy lines) for $(n = 1, f = 2.5\text{--}3.0 \text{ mHz})$, $(n = 1, f = 4.5\text{--}5.0 \text{ mHz})$, and $(n = 2, f = 4.0\text{--}4.5 \text{ mHz})$ and the corresponding predictions (forward models, shown in light lines) from the inversion result. The order of the line styles is solid, dashed, dot-dashed. The noise level in the travel-time measurements can be seen in the small-scale variations.

Appendix: Sound-Speed Kernels for Local Control Measurements

Birch, Kosovichev, and Duvall (2004) used the approach of Gizon and Birch (2002) to derive the sensitivity of time–distance travel-time shifts to local changes in sound speed. In this Appendix, we show that this result can be generalized to the case of travel-time shifts measured from local control correlations.

Assume that we have a model $m(\mathbf{r}, z)$ for the fractional change in the square of the sound speed as a function of horizontal position $[\mathbf{r}]$ and height $[z]$. We would like to obtain the sensitivity functions (kernels) $[K]$ that satisfy

$$\delta\tau(\mathbf{r}) = \iiint K(\mathbf{r}' - \mathbf{r}; z)m(\mathbf{r}', z) d\mathbf{r}' dz, \tag{4}$$

where $\delta\tau(\mathbf{r})$ is the mean travel-time shift (the average of the ingoing and outgoing travel-time shifts) measured from the center–annulus local control correlation with center located at horizontal position \mathbf{r} .

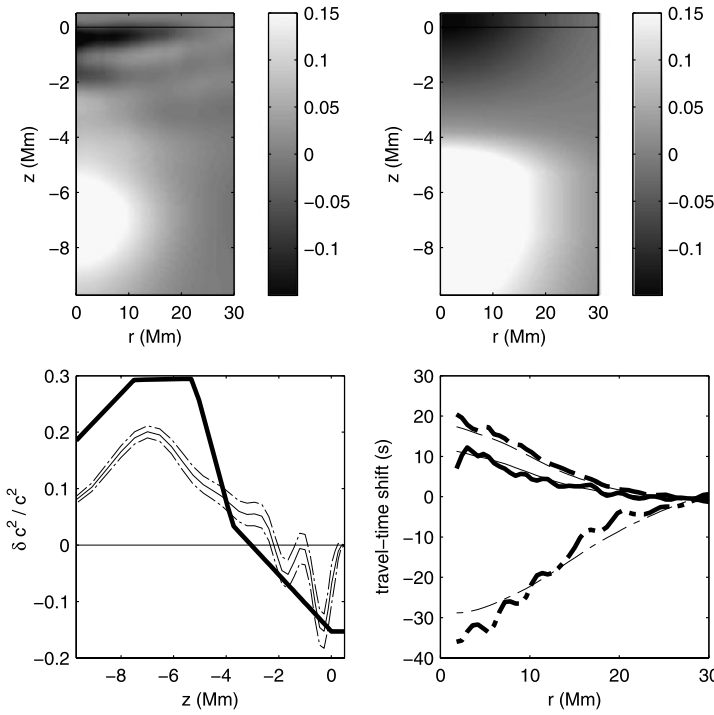


Figure 11 Comparison of an inversion solution with the true two-layer model for the case of the phase-speed filtered measurements and $(\lambda_1, h_k \lambda_2) = (0.1, 0.1) \text{ Mm}^{-1/2}$. The top-left panel shows the azimuthal average of the inversion result. The top-right panel show the true model. The bottom-left panel shows the inferred model (light line) and true model (heavy line) at the center of the “spot” region. The bottom-right panel shows the azimuthal averages of the travel-time maps (heavy lines) for (TD2, $f = 3.5 - 4.0 \text{ mHz}$), (TD2, $f = 4.5 - 5.0 \text{ mHz}$), and (TD5, $f = 5.0 - 5.5 \text{ mHz}$) and the corresponding predictions (forward models, shown in light lines) from the inversion result. The order of the line styles is solid, dashed, dot-dashed.

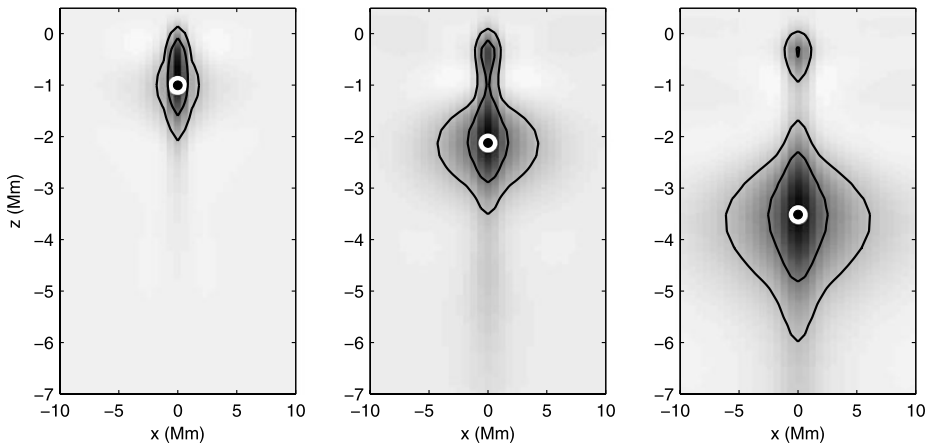


Figure 12 Averaging kernels for the target depths of -1 Mm (left), -2 Mm (middle), and -3.5 Mm (right). The target locations are shown as white circles with an overplotted black dot. The contours show where the averaging kernels have values of 20% and 50% of their maximum. Notice that the averaging kernel for the target depth of 3.5 Mm has a substantial side-lobe near the surface.

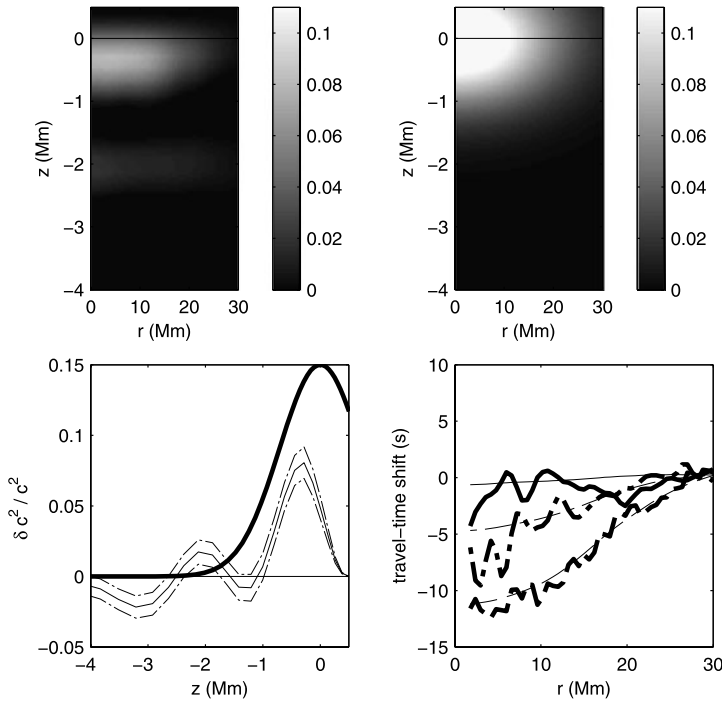


Figure 13 Comparison of an inversion solution with the true one-layer model for the case of the ridge-filtered measurements and $(\lambda_1, h_k \lambda_2) = (0.2, 0.25) \text{ Mm}^{-1/2}$. The top-left panel shows the azimuthal average of the inversion result. The top-right panel show the true model. The bottom-left panel shows the inferred model (light line) and true model (heavy line) at the center of the “spot” region. The bottom-right panel shows the azimuthal averages of the travel-time maps (heavy lines) for $(n = 1, f = 2.5 - 3.0 \text{ mHz})$, $(n = 1, f = 4.5 - 5.0 \text{ mHz})$, and $(n = 2, f = 4.0 - 4.5 \text{ mHz})$ and the corresponding predictions (forward models, shown in light lines) from the inversion result. The order of the line styles is solid, dashed, dot-dashed. The signal-to-noise ratio of the travel-time measurements is much smaller than in the two-layer model.

We begin from the expression relating the local control correlations $[C_{lc}^\pm]$ to the two-point time–distance cross-covariance $[C]$:

$$C_{lc}^\pm(\mathbf{r}, \omega) = \sum_{\mathbf{r}'} G^\pm(\|\mathbf{r}' - \mathbf{r}\|, \omega) C(\mathbf{r}' | \mathbf{r}, \omega) \tag{5}$$

where the sum over horizontal positions $[\mathbf{r}']$ is taken over all grid points where the Green’s function $[G^\pm]$ is not zero and ω is the temporal frequency. For the rest of the [Appendix](#), we assume $\mathbf{r} = \mathbf{0}$ (we can always change the coordinate system such that this is the case, as the reference model for the solar interior is invariant under horizontal translation). Equation (5) shows that changes in the time–distance cross-covariance introduce changes in the local control correlations given by

$$\delta C_{lc}^\pm(\mathbf{0}; \omega) = \sum_{\mathbf{r}} G^\pm(\|\mathbf{r}\|, \omega) \delta C(\mathbf{r}, \omega), \tag{6}$$

where $\delta C(\mathbf{r})$ is the change in the time–distance cross-covariance $C(\mathbf{r} | \mathbf{0})$ and $\delta C_{lc}^\pm(\mathbf{0})$ are the changes in the local control correlations at horizontal position $\mathbf{r} = \mathbf{0}$.

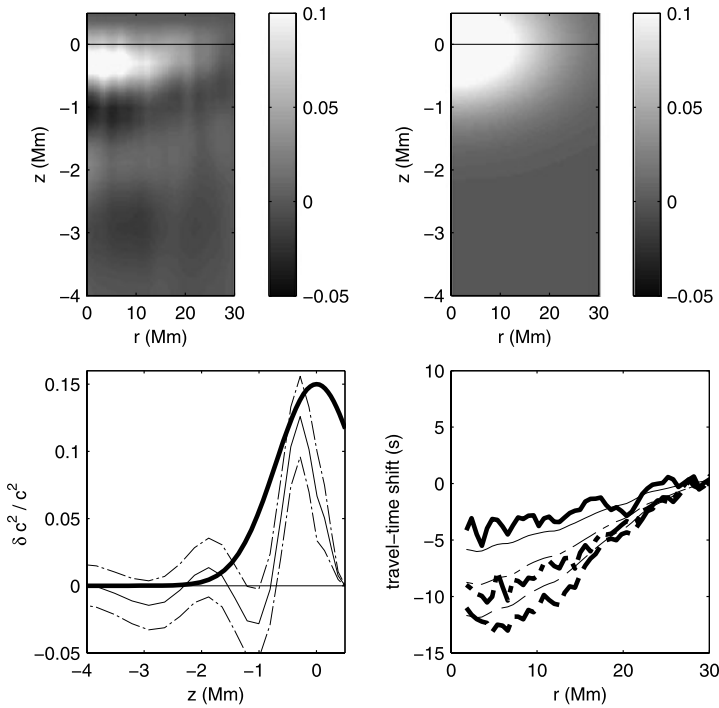


Figure 14 Comparison of an inversion solution with the true one-layer model for the case of the phase-speed filtered measurements for TD1 through TD5 and $(\lambda_1, h_k \lambda_2) = (0.2, 0.1) \text{ Mm}^{-1/2}$. The top-left panel shows the azimuthal average of the inversion result. The top-right panel show the true model. The bottom-left panel shows the azimuthal averages of the travel-time maps (heavy lines) for (TD1, $f = 4.0\text{--}4.5 \text{ mHz}$), (TD2, $f = 5.0\text{--}5.5 \text{ mHz}$), and (TD3, $f = 5.0\text{--}5.5 \text{ mHz}$) and the corresponding predictions (forward models, shown in light lines) from the inversion result. The order of the line styles is solid, dashed, dot-dashed.

Using Equation (6), it is possible to generalize the result of Birch, Kosovichev, and Duvall (2004) to obtain the functions C^\pm that satisfy

$$\delta C_{lc}^\pm(\mathbf{0}; \omega) = \iiint C^\pm(\mathbf{r}, z) m(\mathbf{r}, z) \, d\mathbf{r} \, dz. \tag{7}$$

Using the phase method (*e.g.* Equation (3) of Braun and Birch, 2008), the travel-time shifts $\delta\tau^\pm$ are related to C_{lc}^\pm and δC_{lc}^\pm as

$$\bar{\omega} \delta\tau^\pm = \arg[C_{lc}^\pm + \delta C_{lc}^\pm] - \arg[C_{lc}^\pm], \tag{8}$$

where \arg denotes the argument of a complex number and $\bar{\omega}$ is the mean frequency. In the limit that δC_{lc}^\pm is very small compared to C_{lc}^\pm and that we are working over a narrow range of frequency, we have

$$\delta\tau^\pm = \frac{\text{Im}[C_{lc}^{\pm*} \delta C_{lc}^\pm]}{\bar{\omega} \|C_{lc}^\pm\|^2} \tag{9}$$

where $\text{Im}[\cdot]$ denotes the imaginary part. The shift in the mean travel time is then

$$\delta\tau = [\delta\tau^+ + \delta\tau^-]/2. \quad (10)$$

References

- Basu, S., Antia, H.M., Bogart, R.S.: 2004, Ring-diagram analysis of the structure of solar active regions. *Astrophys. J.* **610**, 1157–1168. doi:[10.1086/421843](https://doi.org/10.1086/421843).
- Birch, A.C., Kosovichev, A.G., Duvall, T.L. Jr.: 2004, Sensitivity of acoustic wave travel times to sound-speed perturbations in the solar interior. *Astrophys. J.* **608**, 580–600. doi:[10.1086/386361](https://doi.org/10.1086/386361).
- Birch, A.C., Braun, D.C., Hanasoge, S.M., Cameron, R.: 2009, Surface-focused seismic holography of sunspots: II. Expectations from numerical simulations using sound-speed perturbations. *Solar Phys.* **254**, 17–27. doi:[10.1007/s11207-008-9282-9](https://doi.org/10.1007/s11207-008-9282-9).
- Bogart, R.S., Basu, S., Rabello-Soares, M.C., Antia, H.M.: 2008, Probing the subsurface structures of active regions with ring-diagram analysis. *Solar Phys.* **251**, 439–451. doi:[10.1007/s11207-008-9213-9](https://doi.org/10.1007/s11207-008-9213-9).
- Braun, D.C., Birch, A.C.: 2006, Observed frequency variations of solar p-mode travel times as evidence for surface effects in sunspot seismology. *Astrophys. J. Lett.* **647**, L187–L190. doi:[10.1086/507450](https://doi.org/10.1086/507450).
- Braun, D.C., Birch, A.C.: 2008, Surface-focused seismic holography of sunspots: I. Observations. *Solar Phys.* **251**, 267–289. doi:[10.1007/s11207-008-9152-5](https://doi.org/10.1007/s11207-008-9152-5).
- Cameron, R.H., Gizon, L., Schunker, H., Pietarila, A.: 2011, Constructing semi-empirical sunspot models for helioseismology. *Solar Phys.* **268**, 293–308. doi:[10.1007/s11207-010-9631-3](https://doi.org/10.1007/s11207-010-9631-3).
- Christensen-Dalsgaard, J., Dappen, W., Ajukov, S.V., Anderson, E.R., Antia, H.M., Basu, S., Baturin, V.A., Berthomieu, G., Chaboyer, B., Chitre, S.M., Cox, A.N., Demarque, P., Donatowicz, J., Dziembowski, W.A., Gabriel, M., Gough, D.O., Guenther, D.B., Guzik, J.A., Harvey, J.W., Hill, F., Houdek, G., Iglesias, C.A., Kosovichev, A.G., Leibacher, J.W., Morel, P., Proffitt, C.R., Provost, J., Reiter, J., Rhodes, E.J., Rogers, F.J., Roxburgh, I.W., Thompson, M.J., Ulrich, R.K.: 1996, The current state of solar modeling. *Science* **272**, 1286–1292.
- Couvidat, S., Birch, A.C.: 2006, Optimal Gaussian phase-speed filters in time–distance helioseismology. *Solar Phys.* **237**, 229–243. doi:[10.1007/s11207-006-0209-z](https://doi.org/10.1007/s11207-006-0209-z).
- Couvidat, S., Rajaguru, S.P.: 2007, Contamination by surface effects of time–distance helioseismic inversions for sound speed beneath sunspots. *Astrophys. J.* **661**, 558–567. doi:[10.1086/515436](https://doi.org/10.1086/515436).
- Couvidat, S., Birch, A.C., Kosovichev, A.G.: 2006, Three-dimensional inversion of sound speed below a sunspot in the Born approximation. *Astrophys. J.* **640**, 516–524. doi:[10.1086/500103](https://doi.org/10.1086/500103).
- Couvidat, S., Gizon, L., Birch, A.C., Larsen, R.M., Kosovichev, A.G.: 2005, Time–distance helioseismology: inversion of noisy correlated data. *Astrophys. J. Suppl.* **158**, 217–229. doi:[10.1086/430423](https://doi.org/10.1086/430423).
- Couvidat, S., Zhao, J., Birch, A.C., Kosovichev, A.G., Duvall, T.L., Parchevsky, K., Scherrer, P.H.: 2010, Implementation and comparison of acoustic travel-time measurement procedures for the solar dynamics observatory/helioseismic and magnetic imager time–distance helioseismology pipeline. *Solar Phys.* doi:[10.1007/s11207-010-9652-y](https://doi.org/10.1007/s11207-010-9652-y).
- Crouch, A.D., Cally, P.S., Charbonneau, P., Braun, D.C., Desjardins, M.: 2005, Genetic magnetohelioseismology with Hankel analysis data. *Mon. Not. Roy. Astron. Soc.* **363**, 1188–1204. doi:[10.1111/j.1365-2966.2005.09515.x](https://doi.org/10.1111/j.1365-2966.2005.09515.x).
- Duvall, T.L., Kosovichev, A.G., Scherrer, P.H., Bogart, R.S., Bush, R.I., de Forest, C., Hoeksema, J.T., Schou, J., Saba, J.L.R., Tarbell, T.D., Title, A.M., Wolfson, C.J., Milford, P.N.: 1997, Time–distance helioseismology with the MDI instrument: initial results. *Solar Phys.* **170**, 63–73.
- Fan, Y., Braun, D.C., Chou, D.: 1995, Scattering of p-modes by sunspots. II. Calculations of phase shifts from a phenomenological model. *Astrophys. J.* **451**, 877–888. doi:[10.1086/176273](https://doi.org/10.1086/176273).
- Gizon, L., Birch, A.C.: 2002, Time–distance helioseismology: the forward problem for random distributed sources. *Astrophys. J.* **571**, 966–986. doi:[10.1086/340015](https://doi.org/10.1086/340015).
- Gizon, L., Birch, A.C.: 2004, Time–distance helioseismology: noise estimation. *Astrophys. J.* **614**, 472–489. doi:[10.1086/423367](https://doi.org/10.1086/423367).
- Gizon, L., Birch, A.C.: 2005, Local helioseismology. *Living Rev. Solar Phys.* **2**, 6 <http://www.livingreviews.org/lrsp-2005-6/>.
- Gizon, L., Birch, A.C., Spruit, H.C.: 2010, Local helioseismology: three-dimensional imaging of the solar interior. *Annu. Rev. Astron. Astrophys.* **48**, 289–338. doi:[10.1146/annurev-astro-082708-101722](https://doi.org/10.1146/annurev-astro-082708-101722).
- Gizon, L., Schunker, H., Baldner, C.S., Basu, S., Birch, A.C., Bogart, R.S., Braun, D.C., Cameron, R., Duvall, T.L., Hanasoge, S.M., Jackiewicz, J., Roth, M., Stahn, T., Thompson, M.J., Zharkov, S.: 2009, Helioseismology of sunspots: a case study of NOAA region 9787. *Space Sci. Rev.* **144**, 249–273. doi:[10.1007/s11214-008-9466-5](https://doi.org/10.1007/s11214-008-9466-5).

- Gough, D.O., Thompson, M.J.: 1991, In: Cox, A.N., Livingston, W.C., Matthews, M.S. (eds.) *Solar Interior and Atmosphere*, University of Arizona Press, Tucson, 519–561.
- Jackiewicz, J., Gizon, L., Birch, A.C.: 2008, High-resolution mapping of flows in the solar interior: fully consistent OLA inversion of helioseismic travel times. *Solar Phys.* **251**, 381–415. doi:[10.1007/s11207-008-9158-z](https://doi.org/10.1007/s11207-008-9158-z).
- Jacobsen, B.H., Moller, I., Jensen, J.M., Efferso, F.: 1999, Multichannel deconvolution, MCD, in geophysics and chemistry. *Phys. Chem. Earth* **24**, 215–220.
- Jensen, J.M., Duvall, T.L. Jr., Jacobsen, B.H., Christensen-Dalsgaard, J.: 2001, Imaging an emerging active region with helioseismic tomography. *Astrophys. J.* **553**, L193–L196. doi:[10.1086/320677](https://doi.org/10.1086/320677).
- Kosovichev, A.G.: 1996, Tomographic imaging of the Sun's interior. *Astrophys. J. Lett.* **461**, L55–L57. doi:[10.1086/309989](https://doi.org/10.1086/309989).
- Kosovichev, A.G.: 2009, Photospheric and subphotospheric dynamics of emerging magnetic flux. *Space Sci. Rev.* **144**, 175–195. doi:[10.1007/s11214-009-9487-8](https://doi.org/10.1007/s11214-009-9487-8).
- Kosovichev, A.G.: 2011, Local helioseismology of sunspots: current status and perspectives (invited review). *Solar Phys.* submitted.
- Kosovichev, A.G., Duvall, T.L. Jr.: 2006, Active region dynamics. *Space Sci. Rev.* **124**, 1–12. doi:[10.1007/s11214-006-9112-z](https://doi.org/10.1007/s11214-006-9112-z).
- Kosovichev, A.G., Duvall, T.L. Jr., Scherrer, P.H.: 2000, Time–distance inversion methods and results (invited review). *Solar Phys.* **192**, 159–176.
- Lindsey, C., Braun, D.C.: 2000, Basic principles of solar acoustic holography (invited review). *Solar Phys.* **192**, 261–284.
- Moradi, H., Baldner, C., Birch, A.C., Braun, D.C., Cameron, R.H., Duvall, T.L., Gizon, L., Haber, D., Hanasoge, S.M., Hindman, B.W., Jackiewicz, J., Khomenko, E., Komm, R., Rajaguru, P., Rempel, M., Roth, M., Schlichenmaier, R., Schunker, H., Spruit, H.C., Strassmeier, K.G., Thompson, M.J., Zharkov, S.: 2010, Modeling the subsurface structure of sunspots. *Solar Phys.* **267**, 1–62. doi:[10.1007/s11207-010-9630-4](https://doi.org/10.1007/s11207-010-9630-4).
- Parchevsky, K.V., Kosovichev, A.G.: 2009, Numerical simulation of excitation and propagation of helioseismic MHD waves: effects of inclined magnetic field. *Astrophys. J.* **694**, 573–581. doi:[10.1088/0004-637X/694/1/573](https://doi.org/10.1088/0004-637X/694/1/573).
- Parchevsky, K.V., Zhao, J., Kosovichev, A.G.: 2008, Influence of nonuniform distribution of acoustic wavefield strength on time–distance helioseismology measurements. *Astrophys. J.* **678**, 1498–1504. doi:[10.1086/533495](https://doi.org/10.1086/533495).
- Zhao, J., Kosovichev, A.G.: 2003, Helioseismic observation of the structure and dynamics of a rotating sunspot beneath the solar surface. *Astrophys. J.* **591**, 446–453. doi:[10.1086/375343](https://doi.org/10.1086/375343).
- Zhao, J., Kosovichev, A.G., Duvall, T.L. Jr.: 2001, Investigation of mass flows beneath a sunspot by time–distance helioseismology. *Astrophys. J.* **557**, 384–388. doi:[10.1086/321491](https://doi.org/10.1086/321491).
- Zhao, J., Kosovichev, A.G., Sekii, T.: 2010, High-resolution helioseismic imaging of subsurface structures and flows of a solar active region observed by Hinode. *Astrophys. J.* **708**, 304–313. doi:[10.1088/0004-637X/708/1/304](https://doi.org/10.1088/0004-637X/708/1/304).
- Zhao, J., Parchevsky, K.V., Kosovichev, A.G.: 2011, *Astrophys. J.* submitted.